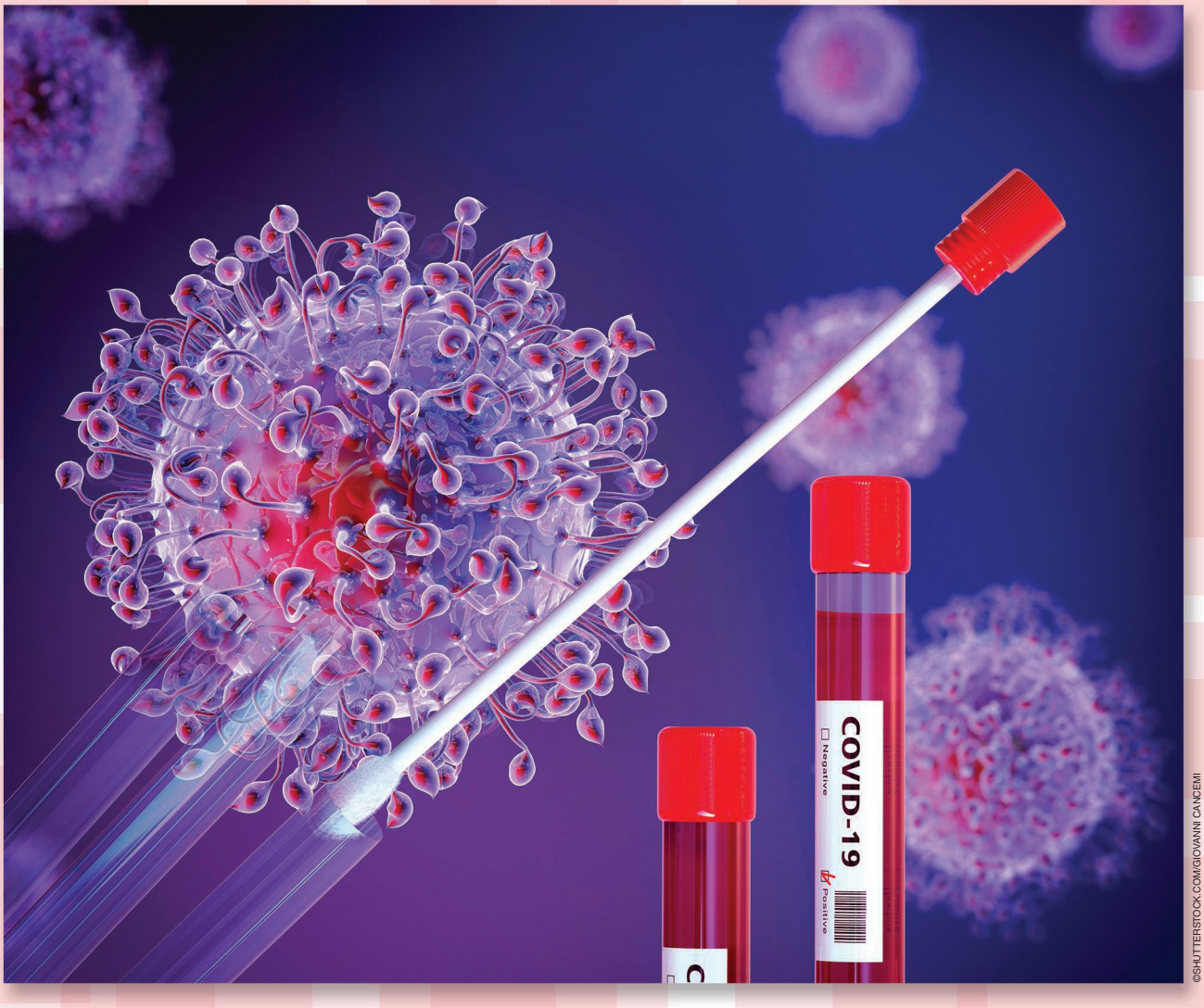

©SHUTTERSTOCK.COM/GIOVANNI CANCEMI

A Tapered Soft Robotic Oropharyngeal Swab for Throat Testing

A New Way to Collect Sputa Samples

Digital Object Identifier 10.1109/MRA.2020.3044914
Date of current version: 25 January 2021

By Zhexin Xie, Bohan Chen, Jiaqi Liu, Feiyang Yuan, Zhuyin Shao, Hui Yang, August G. Domel, Jingfeng Zhang, and Li Wen

The outbreak of COVID-19 has caused immeasurable loss to the world. The highly contagious virus poses a challenging risk to public health, especially medical doctors, who are in close contact with patients. Thus, robots can help reduce the risk of medical professionals conducting massive testing with throat swabs. Soft robots, fabricated with compliant materials, allow for low-cost development and safe interaction with humans and show promising potentiality in testing.

In this article, we developed a new soft robot for effectively collecting pharyngeal samples from the throat (see Figure 1). The robotic prototype consists of a conical-shaped Yoshimura origami as the tip collecting segment and a tapered soft bending actuator as the base to generate motions that mimic a medical doctor's operational movements. Optimized taper angles enhance the elongating and twisting of the origami tip while bending stability is enhanced by the base actuator's tapering shape. The soft robotic swab can achieve rapid (11 s/test) and stable collection with a collecting area up to 218 mm^2.

Through studying the robot's interaction with a 3D printed throat model, the collecting motion (amplitude and frequency) and the force output of the soft robotic swab were similar to a sophisticated medical doctor. We validated the soft robotic swab system with human volunteers and proved its effectiveness. This study provides design insights into creating disposable robotic samplers for an autonomous throat testing system in response to a global epidemic, such as COVID-19.

Background

In 2020, more than 90 million people were infected by COVID-19. This new virus possesses the characteristics of high mortality, infectiousness, and difficulty in detection. Being able to perform rapid testing is essential to cutting virus transmission. As recommended by the World Health Organization, nasopharyngeal swab collection is widely applied for the detection of the virus [1]. Commonly, nurses and doctors stand face-to-face in front of the patients and use a rigid, slim swab to scrape the patients' throats and collect sputa (laryngeal epithelial cells) (see the third section of the supplementary video). Nevertheless, this approach leads to a high-intensity workload and exposes medical workers to the risk of infection. Regarding this risk, developing a robot to replace the medical doctors would be of great benefit.

Existing laryngeal robots apply cotton swabs with rigid sticks and then control the motion of the cotton swab through a rigid robotic arm [2], [3]. There are two primary issues with this rigid robotic approach: 1) the robotic arm mediates the swab movement in front of the patient, and its overall movement causes discomfort [4]; and 2) involuntary movement of the tongue may disturb the swab's motion, resulting in an offset of the collection position. Thus, developing a robotic system that can reduce the patient's concern and efficiently collect throat sputa by preventing the disturbance of the tongue would be essential. Soft materials are flexible, low cost, and safe when interacting with humans [5]–[11]. With these advantages, soft robots have drawn profound interest in medical applications, and existing examples include soft actuators for minimally invasive surgery [12], [13], drug delivery [14], [15], and medical monitoring [16], [17]. These exciting features also provide promising cues for soft robots to be applied to throat testing.

In this work, we developed a soft robotic swab capable of bending, twisting, and elongating to improve patients' comfort. Sampling through a rigid cotton swab relies on the motion of the robotic arm. However, the robotic arm's movement near a human face can cause discomfort and panic [3]. With a soft robotic swab that can be pneumatically actuated to deform inside the human mouth, the robotic arm's movement will no longer be required during the sampling process. The soft robotic swab consists of two components. The first is a Yoshimura origami-based soft collecting segment capable of elongating and twisting. Yoshimura origami structures have been proven to have excellent elongation properties [18], [19], and we improved the origami structure to couple the twisting motion to offer more friction for sampling. The second component is a soft bending actuator capable of horizontal bending to mimic the left–right collecting motion of a medical doctor as well as increase the working stability under a vertical tongue force. Another feature of the soft robotic swab is that the collecting segment and bending

Existing laryngeal robots apply cotton swabs with rigid sticks and then control the motion of the cotton swab through a rigid robotic arm.

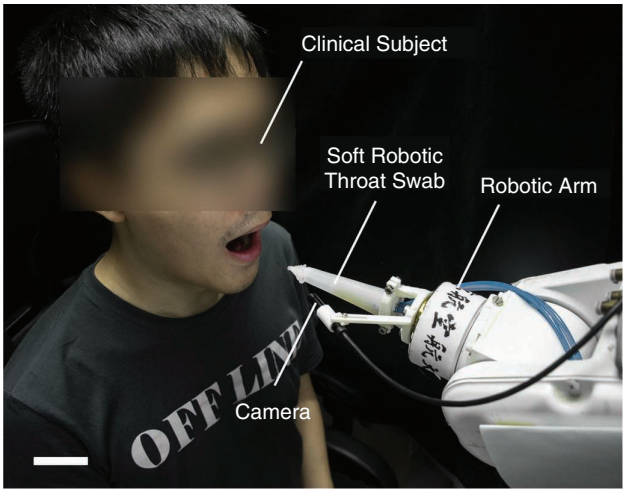

Figure 1. An overview of the soft robotic throat swab system (scale bar = 5 cm).

actuator are designed to be tapered, similar to a cephalopod's arm [20]. We expected this tapered design to endow the robot with the flexibility and robustness necessary to collect throat sputa adequately.

In this research, we first studied the elongating and twisting kinematics of the tapered Yoshimura origami collecting segment and then analyzed the tapered bending actuator's motion stability. Then, we compared the collecting movement and applied force to the soft swab with an experienced doctor on a throat model. Finally, we integrated the soft swab with a commercial robotic arm and camera to implement a complete testing system and tested it on human volunteers. This study provides the first example of applying soft robotics to throat testing and paves the way for the rapid, autonomous testing of COVID-19.

Materials and Methods

Design and Fabrication of the Prototype

The soft robotic swab is composed of two parts: the elongate–twist collecting segment for direct sputa collecting [Figure 2(a) (blue frame)] and the bending actuator for back-end driving [Figure 2(a) (green frame)].

Design of the Collecting Segment

To achieve better scrape performance, we designed the segment using a Yoshimura origami structure. With the extension, the segment can reach the throat of the patient and collect the necessary sputa samples. Considering the size of an adult human throat, we designed a small hemispheric tip (with a diameter of 4 mm) for sputa collecting. We designed the Yoshimura origami structure with a taper angle β to have a thicker collecting segment base for better stability during the extending process.

As seen in Figure 2(b), the conical-shaped Yoshimura origami structure has a basic origami unit (as framed in red). The isosceles angle of the upper rectangle (β_1) is smaller than the lower rectangle (β_2). We folded these rectangles along the intersecting lines to make the origami structure and then contorted the structure by 180° to form the collecting segment structure; the origami segment was then 3D printed in a contorted state. Figure 2(c) illustrates the contorting details of the origami structure; as the top and front views depict, when pneumatically actuated, the origami structure deforms back to the original shape, thus yielding twisting $(\Delta\theta)$ and elongation (Δh).

Figure 3(a)–(c) depicts a portion of the conical-shaped Yoshimura origami structured collecting segment, and the design parameters are given in the image. The folded structure is determined by three vertically arranged concentric equilateral triangles with side lengths of l_t, l_m, and l_b, represented separately by red, green, and blue in the image. The vertical distance between two adjacent equilateral triangles

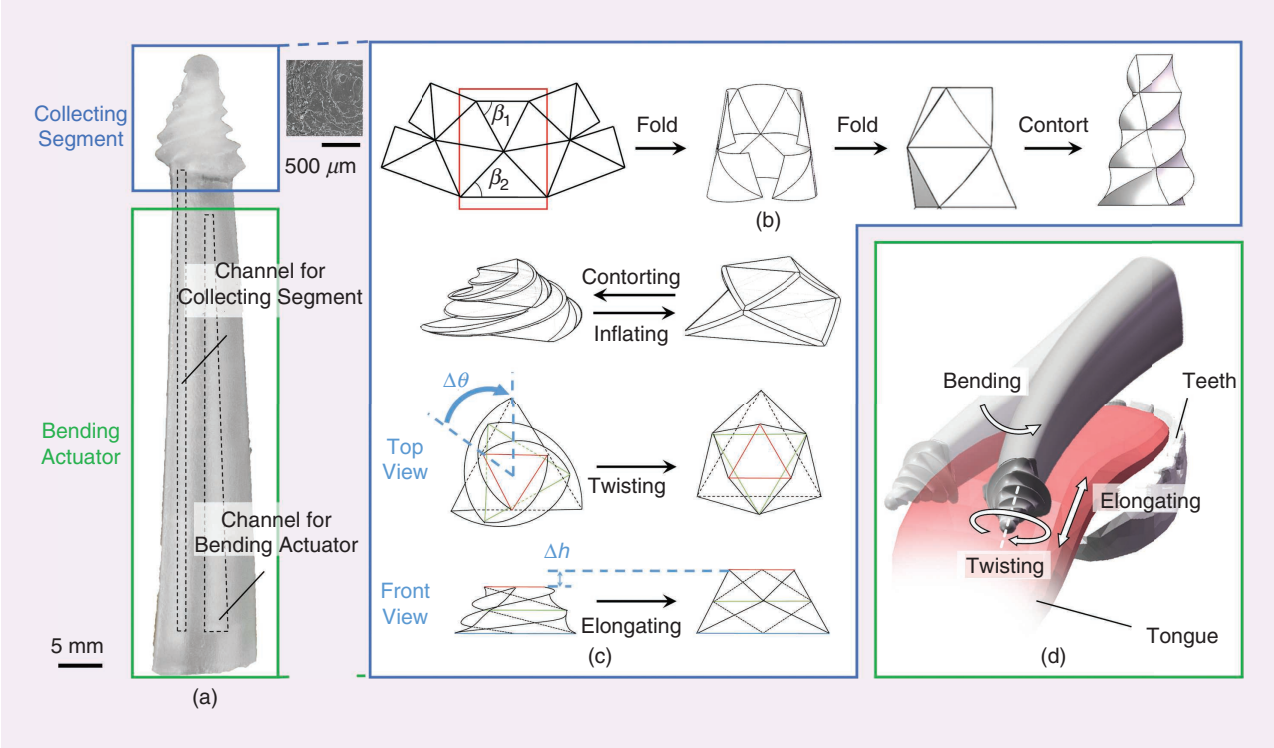

Figure 2. The design principles and motions of the soft robotic swab. (a) The soft robotic swab is composed of two components, a collecting segment and bending actuator. The actuating channels are indicated with dashed lines. The ESEM image illustrates the surface properties of the 3D printed swab. (b) The design process of the origami structure of the collecting segment. The basic rectangle unit of the Yoshimura origami structure is framed in red. (c) By contorting the origami structure, the collecting segment yields a twisting and elongating motion when inflating. (d) The bending actuator bends horizontally when inflating, and the bending displacement direction is marked. ESEM: environmental scanning electron microscope.

is set as $h = 4$ mm. For the top layer of the collecting segment, l_t is the side length of the inner equilateral triangle of the hemispheric tip (diameter 4 mm), and we have $l_t = 4/\sqrt{3}$ mm. The green triangle is oriented opposite to the red and blue ones to simplify the geometric design, and the side length of the green triangle is defined as

$$l_m = \frac{l_t + l_b}{2}. \tag{1}$$

Using the Pythagorean theorem, we have

$$\left(\frac{l_m}{\sqrt{3}} - \frac{l_t}{\sqrt{3}}\right)^2 + h^2 = (l_t \tan\beta_1)^2, \tag{2}$$

$$\left(\frac{l_m}{\sqrt{3}} - \frac{l_b}{\sqrt{3}}\right)^2 + h^2 = (l_b \tan\beta_2)^2. \tag{3}$$

The taper angle β of the conical-shaped Yoshimura origami is defined in Figure 3(c) as

$$\tan\beta = \frac{l_b - l_t}{4h}. \tag{4}$$

With (1)–(4), we have l_m, l_b, β_2, and β uniquely determined once β_1 is given. In this study, we considered a taper angle β from 10 to 35°, with an interval of 5°. We considered the range of 10 to 35° because small angles (<10°) make the collecting segment too thin to keep it stable and large angles (>35°) make the segment's base too thick to be dexterous in a patient's mouth.

The wall thickness of the collecting segment was chosen to be 1 mm, considering the twisting and elongation performance as well as the 3D printing resolution (the smallest printable layer of the 3D printer is 1 mm).

Design of the Bending Actuator

Figure 2(d) displays the actuator's bending motion as well as the elongating and twisting direction of the collecting segment when inflating. In addition to the functionality of depressing the tongue from disturbing the sample collection of the collecting segment, the bending actuator should be able to bend horizontally to enlarge the sampling area, thus achieving sufficient sputa sampling.

The bending actuator was designed to have a semicircular cross-sectional shape. This unique feature endows the soft actuator with low stiffness in the horizontal plane (easier bending) while allowing for higher stiffness in the vertical plane (depressing the tongue) [Figure 3(d)] [20]. The tip size of the bending actuator (a semicircle with a diameter of $D_{tip} = 13$ mm) was determined to match the base of the collecting segment for continuity in the robot. The length of the bending actuator was determined to be sufficient to reach the throat of a patient ($L = 80$ mm) [21].

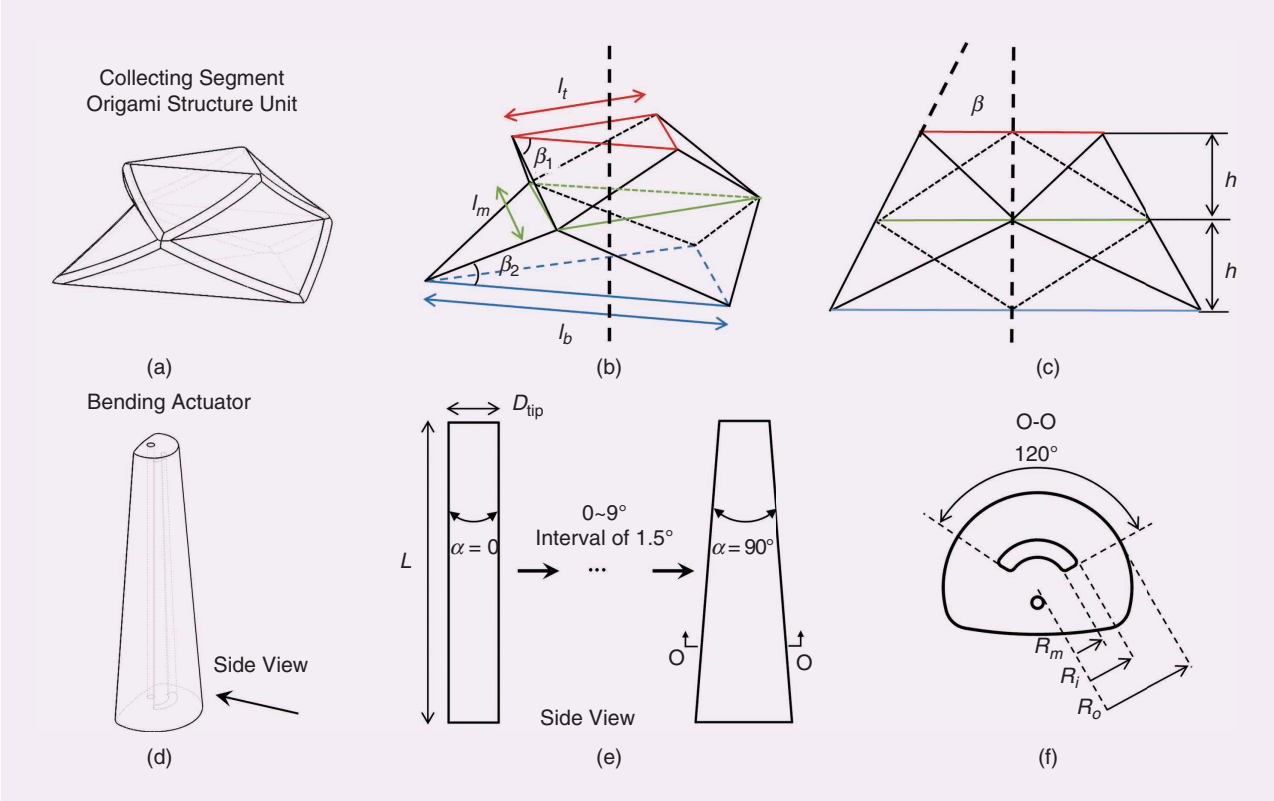

Figure 3. The design parameters of the collecting segment and bending actuator. (a) The collecting segment origami structure unit. (b) and (c) The collecting segment origami geometries. (d) The bending actuator structure. (e) A side view of bending actuators with a taper angle from 0 to 9°. (f) A cross-sectional view of the bending actuator. O-O represents the cross-sectional view at the area marked with O.

To achieve better stability under the force of a patient's tongue, we investigated the effect of the taper angle. We considered taper angles α from 0 to 9°, with an interval of 1.5° [Figure 3(e)]. As the cross-sectional view in Figure 3(f) indicates, an internal chamber was placed along the actuator's length at a fixed normalized distance from the actuator's outer radius $R_0 = 2R_i = 3R_m$ to induce bending via inflation. The chamber was tapered in the same manner as that of the actuator, and the cross-sectional shape of the chamber was annular, with a swept angle of 120° [20]. Meanwhile, a circular channel was placed at the other side of the actuator for inflating the collecting segment.

The optimized model of the soft robotic swab was printed using an Objet Connex500 C3 3D printer. The material selected to fabricate the soft swab was Agilus30, which is soft (Young's modulus 0.66 MPa), nontoxic, and harmless to humans.

Design Space Exploration

To optimize the origami collecting segment and bending actuator's design parameters, we investigated the kinematic motion using the commercially available finite element (FE) software Abaqus. For the bending actuator, we explored the effect of the taper angle on bending amplitude and the capability to resist disturbance from a simulated tongue force. For the origami collecting segment, we studied the effect of the taper angle on both elongation and twist angle.

For the FE studies, all of the models were constructed using 10-node quadratic tetrahedron elements (Abaqus element type C3D10H). The material behavior was captured using an incompressible Gent model [22] with an initial shear modulus μ = 195 kPa and a stiffening parameter J_m = 12 [20]. We first studied the effect of the taper angle β on the origami collecting segment's elongation and twisting angle. For each taper angle β, the collecting segments were pressurized from $P_1 = 0$ to 100 kPa, with intervals of 10 kPa. While studying the effect of the taper angle α on the bending actuator's lateral displacement at the swab tip [see Figure 4(a)], for each taper angle α, the bending actuator was pressurized from P_2 = 0 to 120 kPa at intervals of 10 kPa.

The actuators were placed horizontally (with the actuator base fixed) to assess the taper angle's effect on the capability of resisting tongue disturbance. A simulated tongue force of 0.2 N [22] was applied vertically on the actuator's middle position. The vertical displacement of the swab tip was measured when the actuator was under free load [Figure 4(b)] and when it was actuated with P_1 = 80 kPa for the collecting segment and P_2 =100 kPa for the bending actuator [Figure 4(c)]. For practical use, we then inserted a plastic sheet (tapered in the same manner as that of the bending actuator with a thickness of 0.4 mm and Young's modulus 3.4 GPa) inside the soft swab prototype [Figure 4(d)] and experimentally tested the vertical displacement of the swab tip with a force transducer, exerting a gradually enlarged force, as Figure 4(d) illustrates.

Comparisons Between the Soft Robot and Medical Doctor

To further explore the application of our soft robotic swab design, we compared the motion and applied force of our robot to that of a rigid swab used by an expert medical doctor devoted to COVID-19 virus detection during the early epidemic outbreak in China. The medical doctor used a rigid swab to conduct the sample collection on the 3D printed throat model. A six-axis force transducer was connected to the throat model for applied force acquisition. Simultaneously, a high-speed camera (250 fps) was used to record the motion of the hand movements of the medical doctor. The soft swab was tested in the same manner.

Results

Kinematics of the Tapered Origami Collecting Segment

Figure 5(a) illustrates the effect of the taper angle β and pneumatic pressure on the segment's elongation in the numerical environment. It can be observed that the collecting segment with a taper angle of β = 30° yields the maximum elongation. For example, the elongation increases from 1.18 to 11.07 mm by increasing the pneumatic pressure from P_1 = 30 to 100 kPa, whereas the collecting segment with taper angle β = 20° yields a final elongation of only 9.06 mm when actuated at pneumatic pressure P_1 = 100 kPa.

From Figure 5(b), the results indicate that the twisting angle of the collecting segments first increases and then levels off to a constant value as the pneumatic pressure increases. The collecting segment with taper angle β = 10° yields the smallest maximum twisting angle, 17.39°, while the collecting segments with a taper angle from 15 to 35° all generate twisting angles around 18.15° (β = 30°, P_1 = 100 kPa). Therefore, taking both elongation and twisting performance into account, we chose a taper angle β = 30° to fabricate and test the collecting segment [Figure 5(f)]. The results [Figure 5(d) and (e)] indicate good agreement between the simulations and experiments. Figure 5(c) and (f) displays the elongation and twisting motion of both the simulated and real collecting segments actuated by pneumatic pressure P_1 from 0 to 80 kPa. Once again, there is a good agreement between the simulation and experiment.

Kinematics of the Tapered Bending Actuator

We also considered the effect of the taper angle on the bending ability. As Figure 4(a) indicates, the results demonstrate that the bending distance of the bending actuator increases as pressure P_2 increases but decreases slightly as the taper angle α increases. For example, the bending distance decreases from 19.51 to 13.38 mm by increasing the taper angle α from 0 to 9° at P_2 = 120 kPa, and it changes from 0.55 to 13.38 mm by increasing the pressure P_2 from 40 to 120 kPa.

We next investigated the capability of resisting tongue disturbance. As Figure 4(b) demonstrates, the numerical results indicate that the taper angle plays a notable role in

weakening the interference of the tongue force. For example, the tip displacement decreases from 39.70 to 4.00 mm under the simulated tongue force (0.2 N) when the taper angle α increases from 0 to 9°. For the pneumatically actuated prototype, we inflated the bending actuator (P_2 = 100 kPa) and collecting segment (P_1 = 80 kPa). From Figure 4(c), when the taper angle α increases from 0 to 9° for the actuated prototype, the tip displacement decreases from 44.31 to 5.20 mm under the simulated tongue force. As Figure 4(b) and (c) illustrates, we conclude that the offset of the soft bending actuator with a taper angle of 9° is quite small during operation under the simulated tongue force. After inserting a piece of plastic sheet in the prototype with a taper angle of 9°, we found that the soft swab can endure a tongue force as large as 2.5 N and the tip displacement decreases to 5.36 mm, allowing for stable application.

From discussions with a clinical doctor working with COVID-19 patients, a horizontal motion of ~1 cm of the cotton swab in the throat can achieve valid sputa collection [the black dashed line in Figure 4(a)]. Taking both the bending and disturbance resisting abilities into account, we chose the soft robotic throat swab with a taper angle α = 9° to achieve stable manipulation even under tongue force while still having sufficient workspace within the patient's throat.

Testing on the Throat Model

Guided by these numerical results, we next were interested in how the soft robot engages with a throat model. We fabricated

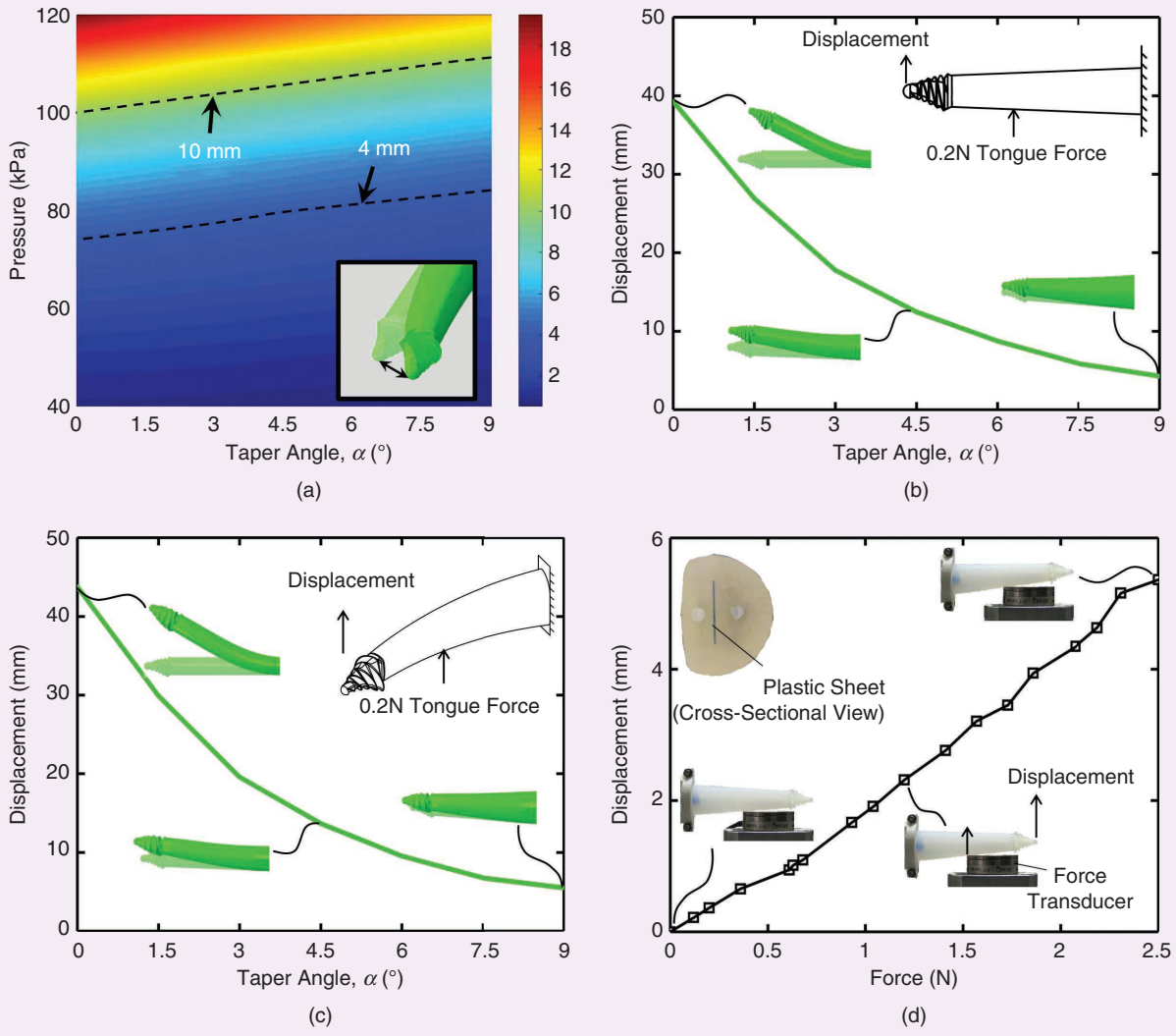

Figure 4. Modeling the effects of the bending actuator taper angle on the bending distance and capability of resisting tongue disturbance. (a) The numerical results illustrating the bending distance as a function of the taper angle (α) and actuation pressure (P_1). The heat map was interpolated with the griddata() function in Matlab (with an interval taper angle of 1.5°). The numerical results illustrating the tip offset under tongue force (0.2 N) as a function of the taper angle (α) when (b) the prototype is freely placed and (c) kept actuated with P_1 =100 kPa for the bending actuator and P_2 = 80 kPa for the collecting segment. (d) The experimental results of tip offset of the plastic sheet inserted prototype under tongue force from 0 to 2.5 N.

More than 90% of the tested subjects said that the soft robotic swab would not reduce comfort compared with the cotton swab.

the soft robotic swab with a collecting segment taper angle $\beta = 30°$ and a bending actuator taper angle $\alpha = 9°$. We then explored the interaction of the soft robot with the throat through both FE simulations and experimental conditions.

For the FE simulations, we considered the collecting segment touching a human palatoglossal arch [the blue section in Figure 6(a)]. The material was modeled as a linear elastic material with Young's modulus of 1.3 MPa, which is close to the modulus of palatoglossal arch tissue while the mouth is open [21], [23]. The collecting segment [Figure 6(a), green part] was placed in front of the palatoglossal arch model and actuated with pressure from 0 to 100 kPa. Figure 6(a) indicates that, with increasing pneumatic pressure, the collecting segment elongates and slips down along the palatoglossal arch, generating a scraping motion on the surface. The stress distribution of this scraping is displayed in Figure 6(a).

Then, we explored the scraping area of the soft robotic swab via frustrated total internal reflection (FTIR) [24] on a translucent acrylic plate. Figure 6(b) depicts the three working stages. First, the hemispheric tip scraped down on the plate surface when inflating the collecting segment (P_1 = 80 kPa). Second, the collecting segment released, and the bending actuator was inflated to move the sampling area horizontally. Third, the collecting segment was inflated again to repeat the collecting motion. By calculating the white pixel numbers of the binary processed FTIR images, the scrape area of the soft robotic swab is enlarged from 122 (no bending) to 218 mm^2 (with bending). More details of the whole process are available in the second section of the supplementary video.

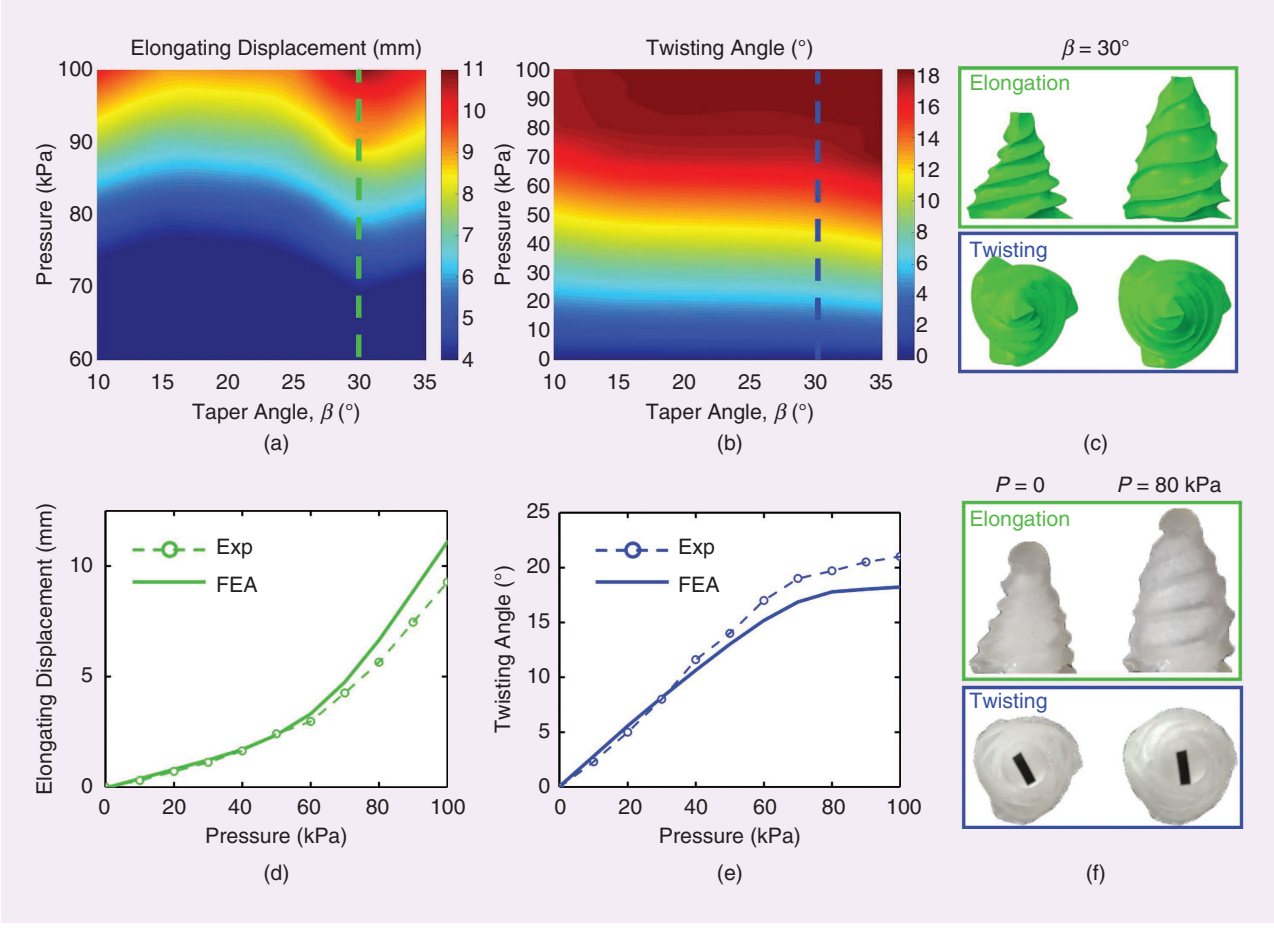

Figure 5. Modeling the effects of the collecting segment taper angle on elongating and twisting. (a) The numerical results illustrating the elongation as a function of the taper angle (β) and input pressure (P_1). (b) The numerical results illustrating the twisting angle as a function of the taper angle (β) and input pressure (P_1). The front and top views present good structural agreement between the simulated (c) and real experimental (f) collecting segment with a taper angle $\beta = 30°$ when actuated by pneumatic pressure P_1 ranging from 0 to 80 kPa. (d) Elongation and (e) twisting angle comparisons show good agreement between the simulation and experimental results of the collecting segment with taper angle $\beta = 30°$. See the first section of the supplementary video for more motion details. Exp: experimental; FEA: finite element analysis.

Comparison Between the Soft Robot and Medical Doctor

Figure 7(a) displays the medical doctor scraping the palatoglossal arch part rapidly downward. The corresponding applied force along the x, y, and z axes during that process is represented in Figure 7(b)–(d). The force along the three directions in each case shows a trend of increasing to a peak value and then returning to the relaxed state. We collected $N = 25$ sets of scrape force measurements generated by the medical doctor during the sampling process, the average force of which was 0.31 ± 0.26 N (mean ± standard deviation).

Next, we compared the soft robotic swab's sampling motion at the same palatoglossal arch part. As Figure 7(e) expresses, there are two processes during the sampling motion of the robotic swab. First, the collecting segment was inflated with 80 kPa at 1.1 s, forcing the tip to glide downward with a peak force value at 2.8 s [Figure 7(f)–(h)]. After releasing the collecting segment, the bending actuator was inflated with 100 kPa to achieve a similar downward slope motion to the medical doctor. The force reached another peak value at 4.9 s. The force values of the soft robotic swab (0.41 ± 0.05 N) were slightly larger than those of the medical doctor (0.31 ± 0.26 N). Three repeated trials were conducted. See the third section of the supplementary video for more details of the comparison.

Compared with the sampling motion of the medical worker, our results demonstrate that the motion and applied force of our soft robotic swab are very similar to the doctor's motion, which suggests that our soft robotic swab can accomplish professional medical sample collection.

With permission of research ethics oversight from Beihang University (BM20200179), we conducted the entire sampling process of the soft robotic throat swab system on a human volunteer (Figure 8 and the fourth section of the supplementary video). The process was divided into three steps:

1) The soft swab was moved in front of the patient with the tip facing the mouth (0–3 s). Guided by the feedback of the video camera, the nonpressurized soft swab entered the throat via the motion of the robotic arm (4 s).
2) After arriving at the throat's sampling location, the collecting segment was inflated to scrape the throat for the first collection (5 s). After completing the collection on one side, the collecting segment was released. Then, the soft swab bent horizontally to the sampling point on the other side of the throat (7 s) and scraped for the second collection (8 s).
3) After the collection procedures, the soft swab was unpressurized (10 s) and left the mouth (11 s).

During the process displayed in Figure 8, the volunteer found no discomfort and pharyngeal reflex.

We further recorded 15 human subjects' feelings with both the medical rigid throat swab and our soft robotic swab. One subject preferred the medical rigid throat swab, five subjects preferred the soft robotic swab, and nine subjects thought the two swabs brought similar feelings. More than 90% of the tested subjects said that the soft robotic swab would not reduce comfort compared with the cotton swab.

Discussion and Conclusions

In this article, we proposed a soft robotic throat swab system for sputa collection in the detection of viruses. The soft swab consists of a tapered origami collecting segment and a tapered bending actuator. We used a combination of numerical analyses and experiments to investigate the parametric design of the soft swab. We found that the optimized tapered Yoshimura origami collecting segment yielded appropriate elongation and twisting motions, which allows for effective throat

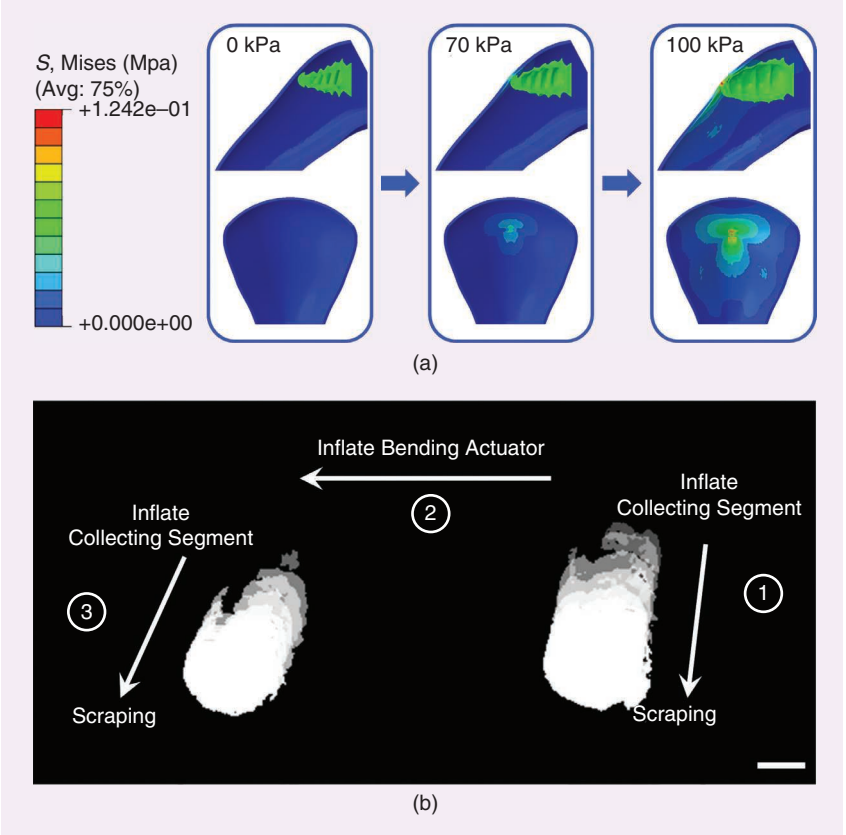

Figure 6. The interaction between the soft robotic swab and throat. (a) The numerical results illustrating that the tip of the robotic swab slips down along the throat surface with the collecting segment elongation. (b) The FITR images highlighting the scraping area range of the soft robotic swab (see the second section of supplementary video). Scale bar = 5 mm. Avg: average; S, Mises: von Mises stress.

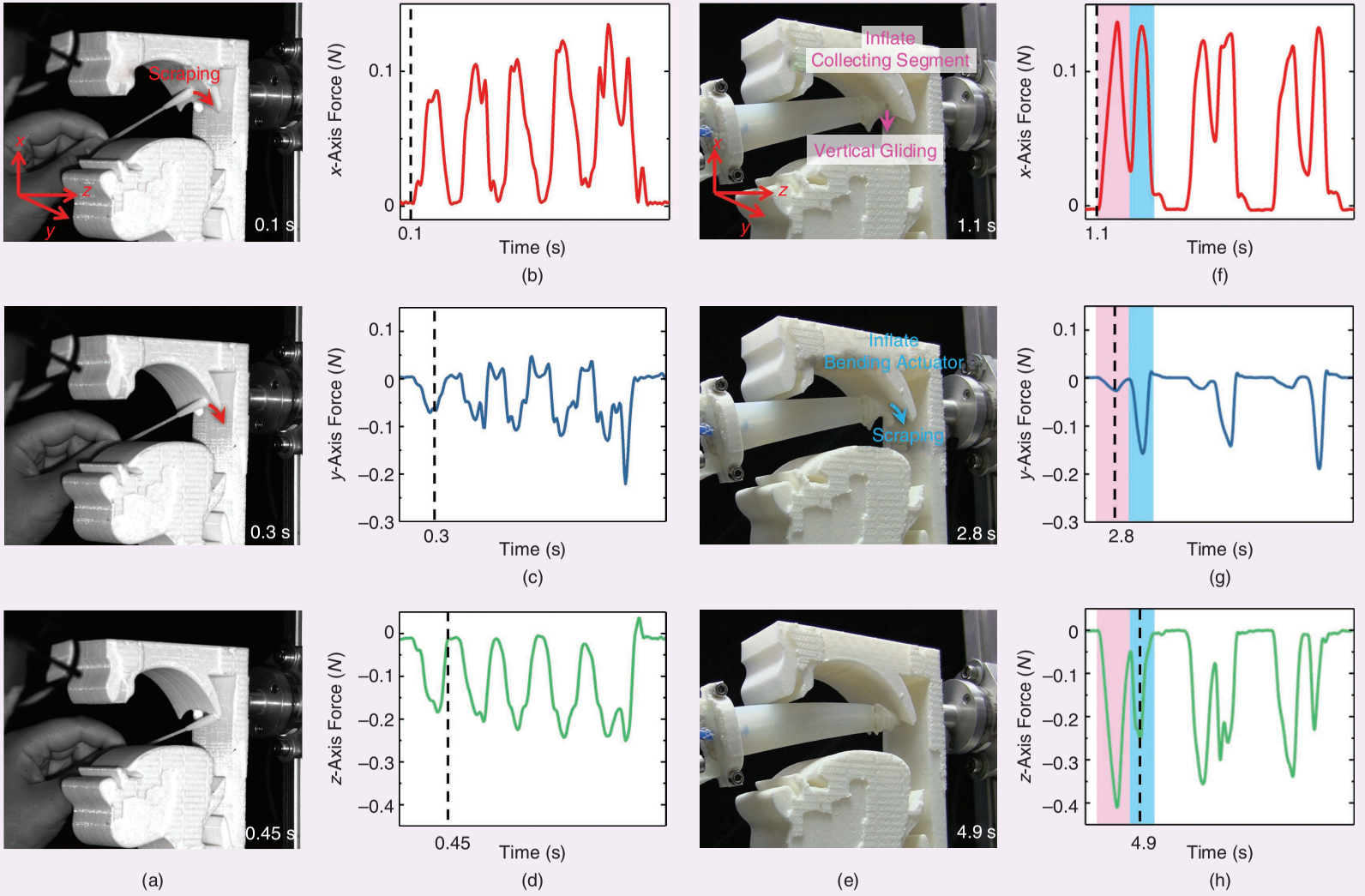

Figure 7. The motion and applied force comparisons between the soft robotic swab and the rigid swab conducted by the medical doctor. (a) The motion of the hand of the doctor recorded by a high-speed camera with 250 fps. (b)–(d) The corresponding applied force of the doctor on the throat model during the collecting action presented in (a). The component forces along the *x, y,* and *z,* axes are given, respectively. (e) The motion of the soft robotic swab. (f)–(h) The corresponding applied force of the soft robotic swab on the throat model during the action presented in (e). The component forces along the *x, y,* and *z,* axes are given, respectively. A comparison is available in the third section of the supplementary video.

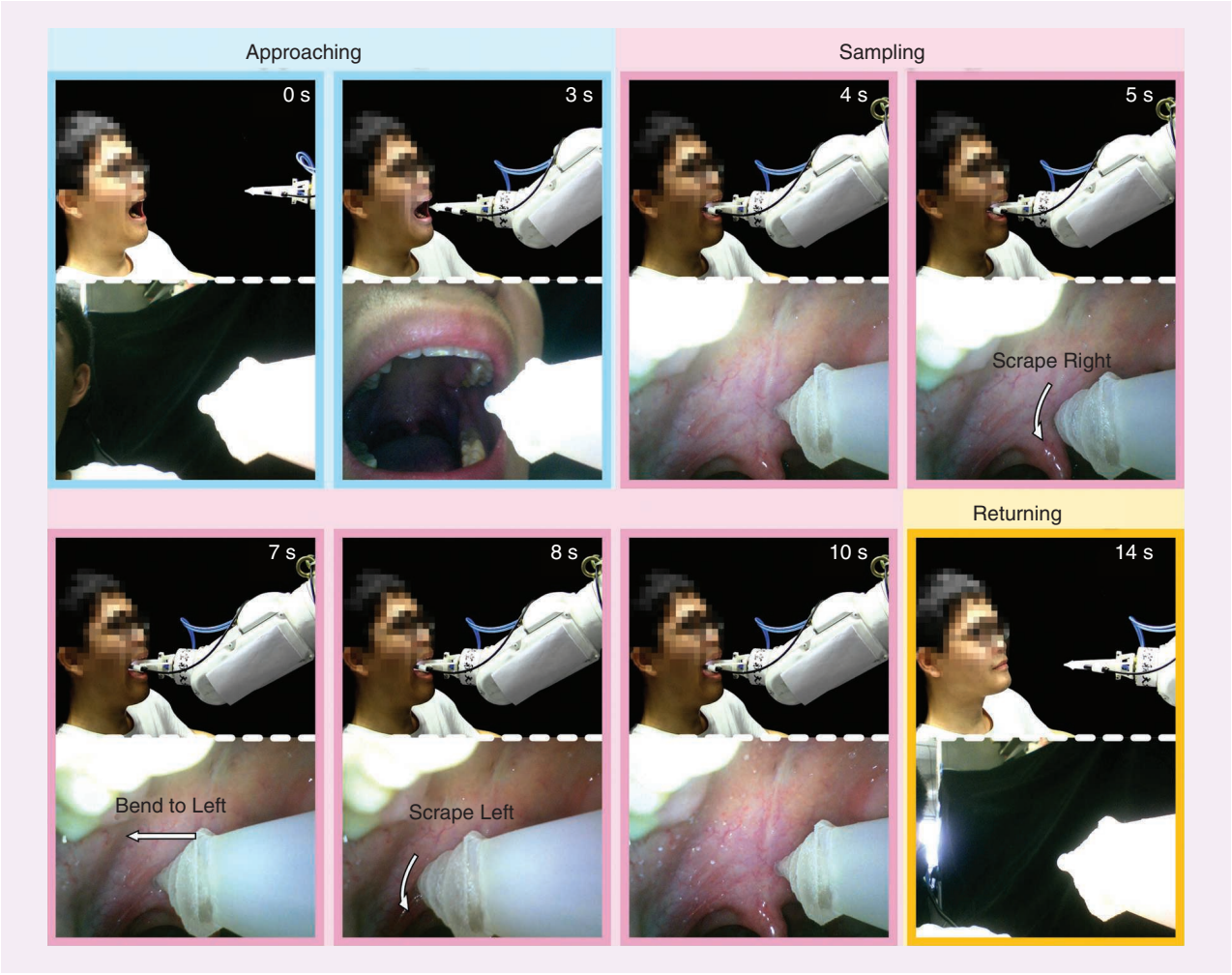

Figure 8. The working process of the soft robotic throat system on a human clinical subject. Blue box: the soft robotics swab enters into the patient's mouth. Red box: the soft robotic swab is actuated to collect sputa samples. Yellow box: the sample collection is completed, and the soft robotic swab leaves the mouth.

scraping and sputa collection. We also found that the tapered bending actuator was able to both depress the simulated interference of the tongue and increase the collection area. Guided by FE analysis, the soft robotic swab design parameters were optimized.

Notably, we found that the bending motion of the bending actuator and the elongating of the collecting segment enable effective scraping of the throat [Figure 6(b)]. With the combined function of bending, elongating, and twisting, our soft swab can achieve a collecting motion and applied force similar to that of a sophisticated medical doctor. Compared with previous studies that use traditional rigid throat swabs composed of a wooden stick [2] or a complex hinge structure that requires accurate control of a robotic arm [3], our soft robotic swab can move and collect sputa with simple pneumatic actuation, helping to alleviate a patient's panic. Tests on human volunteers also demonstrate that this robotic system can achieve a safe and comfortable sampling motion.

Comparison results between the robot and the medical doctor show a few limitations of the current robotic prototype. First, the medical doctor can achieve a much faster sampling speed [~0.5 s/sample, Figure 7(a)] than the soft robot [~5 s/sample, Figure 7(b)]. Second, the collecting segment cannot be dislodged autonomously; further work would be necessary to add this functionality. Note that sanitation plays a crucial role in guaranteeing the biosafety of storage and transportation of the samples for further polymerase chain reaction tests. The modularized design of the collecting segment for sanitation would further complement the prototype.

Acknowledgments

This work was supported by the National Key R&D Program of China (grants 18YFB1304600 and 2019YFB1309600) and by the National Science Foundation support projects, China (grants 91848206, 61822303, 91848105, 61633004, and 92048302). Zhexin Xie is supported by the Academic Excellence Foundation of Beihang University for Ph.D. Students. Li Wen, Zhexin Xie, Bohan Chen, Jingfeng Zhang, and Hui Yang are inventors on the patent application (202010389219.0) submitted by Beihang University that covers the structure design of the soft swab system. Zhexin Xie, Bohan Chen, and Jiaqi Liu contributed equally to this article.

References

[1] World Health Organization. "Laboratory testing for coronavirus disease (COVID-19) in suspected human cases: Interim guidance, 19 March 2020." 2020. World Health Organization. https://apps.who.int/iris/handle/10665/331501 (accessed Jan. 11, 2021).

[2] S. Wang, K. Wang, R. Tang, J. Qiao, H. Liu, and Z. -G. Hou, "Design of a low-cost miniature robot to assist the COVID-19 nasopharyngeal swab sampling," 2020, arXiv:2005.12679.

[3] P. Berthet-Rayne et al., "The i^2 snake robotic platform for endoscopic surgery," *Ann. Biomed. Eng.*, vol. 46, no. 10, pp. 1663–1675, 2018. doi: 10.1007/s10439-018-2066-y.

[4] C. P. Seaman et al., "Self-collected compared with professional-collected swabbing in the diagnosis of influenza in symptomatic individuals: A meta-analysis and assessment of validity," *J. Clin. Virol.*, vol. 118, pp. 28–35, Sept. 2019. doi: 10.1016/j.jcv.2019.07.010.

[5] D. Rus et al., "Design, fabrication and control of soft robots," *Nature*, vol. 521, no. 7553, pp. 467–475, 2015. doi: 10.1038/nature14543.

[6] J. Rossiter and H. Hauser, "Soft robotics—The next industrial revolution," *IEEE Robot. Automat. Mag.*, vol. 23, no. 3, pp. 17–20, 2016. doi: 10.1109/MRA.2016.2588018.

[7] L. Han, H. Wang, Z. Liu, W. Chen, and X. Zhang, "Vision-based cutting control of deformable objects with surface tracking," *IEEE/ASME Trans. Mechatronics*, early access, 2020. doi: 10.1109/TMECH.2020.3029114.

[8] M. Runciman, A. Darzi, and G. P. Mylonas, "Soft robotics in minimally invasive surgery," *Soft Robot.*, vol. 6, no. 4, pp. 423–443, 2019. doi: 10.1089/soro.2018.0136.

[9] S. Zhuo et al., "Complex multiphase organohydrogels with programmable mechanics toward adaptive soft-matter machines," *Sci. Adv.*, vol. 6, no. 5, p. eaax1464, 2020. doi: 10.1126/sciadv.aax1464.

[10] H. Yuk et al., "Dry double-sided tape for adhesion of wet tissues and devices," *Nature*, vol. 575, no. 7781, pp. 169–174, 2019. doi: 10.1038/s41586-019-1710-5.

[11] Z. Xie, F. Yuan, Z. Liu, Z. Sun, E. M. Knubben, and L. Wen, "A Proprioceptive Soft Tentacle Gripper Based on Crosswise Stretchable Sensors," *IEEE/ASME Trans. Mechatronics*, vol. 25, no. 4, pp. 1841–1850, 2020. doi: 10.1109/TMECH.2020.2993258.

[12] H. Gu, H. Wang, F. Xu, Z. Liu, and W. Chen, "Active fault detection of soft manipulator in visual servoing," *IEEE Trans. Ind. Electron.*, early access, 2020. doi: 10.1109/TIE.2020.3028813.

[13] Y. J. Kim, S. Cheng, S. Kim, and K. Iagnemma, "A novel layer jamming mechanism with tunable stiffness capability for minimally invasive surgery," *IEEE Trans. Robot.*, vol. 29, no. 4, pp. 1031–1042, 2013. doi: 10.1109/TRO.2013.2256313.

[14] W. Hu, G. Z. Lum, M. Mastrangeli, and M. Sitti, "Small-scale soft-bodied robot with multimodal locomotion," *Nature*, vol. 554, no. 7690, pp. 81–85, 2018. doi: 10.1038/nature25443.

[15] Y. Kim, G. A. Prada, S. Liu, and X. Zhao, "Ferromagnetic soft continuum robots," *Sci. Robot.*, vol. 4, no. 33, p. eaax7329, 2019. doi: 10.1126/scirobotics.aax7329.

[16] H. U. Chung et al., "Skin-interfaced biosensors for advanced wireless physiological monitoring in neonatal and pediatric intensive-care units," *Nat. Med.*, vol. 26, no. 3, pp. 418–429, 2020. doi: 10.1038/s41591-020-0792-9.

[17] A. D. Mickle et al., "Wireless closed-loop system for optogenetic peripheral neuromodulation," *Nature*, vol. 565, no. 7739, pp. 361–365, 2019. doi: 10.1038/s41586-018-0823-6.

[18] J. Cai, X. Deng, Y. Xu, and J. Feng, "Motion analysis of a foldable barrel vault based on regular and irregular Yoshimura origami," *J. Mech. Robot.*, vol. 8, no. 2, p. 021017, 2016. doi: 10.1115/1.4031658.

[19] R. V. Martinez, C. R. Fish, X. Chen, and G. M. Whitesides, "Elastomeric origami: Programmable paper-elastomer composites as pneumatic actuators," *Adv. Funct. Mater.*, vol. 22, no. 7, pp. 1376–1384, 2012. doi: 10.1002/adfm.201102978.

[20] Z. Xie et al., "Octopus arm-inspired tapered soft actuators with suckers for improved grasping," *Soft Robot.*, vol. 7, no. 5, pp. 639–648, 2020. doi: 10.1089/soro.2019.0082.

[21] B. Gick et al., "Speech function of the oropharyngeal isthmus: A modelling study," *Comput. Methods Biomech. Biomed. Eng. Imaging Vis.*, vol. 2, no. 4, pp. 217–222, 2014. doi: 10.1080/21681163.2013.851627.

[22] A. Gent, "A new constitutive relation for rubber," *Rub. Chem. Tech.*, vol. 69, no. 1, pp. 59–61, 1996. doi: 10.5254/1.3538357.

[23] Y. Huang, D. P. White, and A. Malhotra, "The impact of anatomic manipulations on pharyngeal collapse: Results from a computational model of the normal human upper airway," *Chest*, vol. 128, no. 3, pp. 1324–1330, 2005. doi: 10.1378/chest.128.3.1324.

[24] J. Han, "Low-cost multi-touch sensing through frustrated total internal reflection," in *Proc. 18th Annu. ACM Symp. User Interface Softw. Technol.*, pp. 115–118. 2005. doi: 10.1145/1095034.1095054.

Zhexin Xie, School of Mechanical Engineering and Automation and Shenyuan Honors College, Beihang University, Beijing, 100191, China. Email: zhexinxie@buaa.edu.cn.

Bohan Chen, School of Mechanical Engineering and Automation, Beihang University, Beijing, 100191, China. Email: albertchen@buaa.edu.cn.

Jiaqi Liu, School of Mechanical Engineering and Automation, Beihang University, Beijing, 100191, China. Email: jiaqiliu@buaa.edu.cn.

Feiyang Yuan, School of Mechanical Engineering and Automation, Beihang University, Beijing, 100191, China. Email: feiyangyuan_buaa@163.com.

Zhuyin Shao, School of Mechanical Engineering and Automation, Beihang University, Beijing, 100191, China. Email: szy_hhh@buaa.edu.cn.

Hui Yang, School of Mechanical Engineering and Automation, Beihang University, Beijing, 100191, China. Email: 405377205@qq.com.

August G. Domel, Department of Bioengineering, Stanford University, Stanford, California, 94305, USA. Email: augustdomel@gmail.com.

Jingfeng Zhang, Peking University Third Hospital, Beijing, 100191, China. Email: zjf117333@163.com.

Li Wen, School of Mechanical Engineering and Automation, Beihang University, Beijing, 100191, China, and Beijing Advanced Innovation Center for Biomedical Engineering, Beihang University, Beijing, 100191, China. Email: liwen@buaa.edu.cn.